Sound-speed and attenuation imaging of breast tissue using waveform tomography of transmission ultrasound data

R. Gerhard Pratt[a], Lianjie Huang[b], Neb Duric[c], and Peter Littrup[c]

[a]Queen's University, Kingston, ON, Canada K7L 3N6
[b]Los Alamos National Laboratory, Los Alamos, NM 87545
[c]Karmanos Cancer Institute, 4100 John R., 4HWCRC Detroit, MI 48201-2013

ABSTRACT

Waveform tomography results are presented from 800 kHz ultrasound transmission scans of a breast phantom, and from an in vivo ultrasound breast scan: significant improvements are demonstrated in resolution over time-of-flight reconstructions. Quantitative reconstructions of both sound-speed and inelastic attenuation are recovered. The data were acquired in the Computed Ultrasound Risk Evaluation (CURE) system, comprising a 20 cm diameter solid-state ultrasound ring array with 256 active, non-beamforming transducers.

Waveform tomography is capable of resolving variations in acoustic properties at sub-wavelength scales. This was verified through comparison of the breast phantom reconstructions with x-ray CT results: the final images resolve variations in sound speed with a spatial resolution close to 2 mm.

Waveform tomography overcomes the resolution limit of time-of-flight methods caused by finite frequency (diffraction) effects. The method is a combination of time-of-flight tomography, and 2-D acoustic waveform inversion of the transmission arrivals in ultrasonic data. For selected frequency components of the waveforms, a finite-difference simulation of the visco-acoustic wave equation is used to compute synthetic data in the current model, and the data residuals are formed by subtraction. The residuals are used in an iterative, gradient-based scheme to update the sound-speed and attenuation model to produce a reduced misfit to the data. Computational efficiency is achieved through the use of time-reversal of the data residuals to construct the model updates. Lower frequencies are used first, to establish the long wavelength components of the image, and higher frequencies are introduced later to provide increased resolution.

Keywords: sound-speed, attenuation, waveform tomography, transmission ultrasound, image processing

1. INTRODUCTION

During the past decade much attention has been focused on the use of ultrasound transmission in the early detection and evaluation of breast cancers.[1–5] In contrast to traditional ultrasound methods using reflection and backscattering (or B-mode), transmission ultrasound has the potential of yielding accurate, quantitative sound speed images and attenuation images. This is particularly important as reflection methods are limited by the lack of specular reflectors associated with breast tumors.[5] A ring transducer such as that used in the Computed Ultrasound Risk Evaluation (CURE) system[5,6] (described below) allows the possibility of utilizing both modalities: Transmission information is used to reconstruct sound speed and attenuation images, while backscattered waves supplement these with high resolution migration methods.[7,8]

Sound speed and attenuation images are most often extracted from transmission ultrasound data using "time-of-flight" methods, in which arrival times, amplitudes are extracted, and ray-based inversion methods are used to reconstruct the images. These methods are robust, and rapid*. In general the reconstructions should be performed iteratively to allow the rays to correctly curve within heterogeneous media, although in practice with breast tissue straight rays are often used.[5] Regardless of ray tracing approaches, all image reconstruction methods based on first arrival times are limited in resolution as a result of the relatively long wavelengths of

---

Correspondence to pratt@geol.queensu.ca; phone 613 533 6501
*The current goal for transmission systems is a throughput of 25 patients per day.[5]

ultrasound ($\approx$ 1 mm), and the resulting diffractions that appear in the data. The limitations of traveltime reconstruction methods are well understood, and the methods of diffraction tomography[9, 10] have been proposed as a solution. Just as for ray-based methods, diffraction methods must correctly respect the variations of sound speed within the media, and hence more sophisticated methods not relying on the assumption of homogeneity in the background are required.

In geophysical imaging, similar physical problems arise, and can be shown to have similar scale characteristics. Table 1 shows characteristic scales for the CURE system, and for a recent geophysical study designed to probe the earth's crust and upper mantle.[11, 12] In both cases, the key scale characteristic is the number of wavelengths, N_λ that acoustic energy must propagate from source to receiver locations (of the order of 100). Scatterers of the order of the wavelength, λ (i.e., of the order millimeters in the medical ultrasound case) will strongly diffract energy and obscure the first arrivals, making traveltimes less diagnostic of small scale variations in sound speed and attenuation. In geophysical imaging there are no alternative modalities - acoustic energy offers the optimal imaging technology[†], and geophysical imaging algorithms exist that overcome the limitations of time-of-flight, ray-based methods. Due to the strong variations in sound speed for most earth materials, these algorithms correctly take into account heterogeneity. To some extent geophysical algorithms also overcome some of the difficulties of irregular and poorly sampled wavefields. It is therefore appropriate to investigate the applicability of geophysical imaging methods to the medical ultrasound transmission problem.

Table 1. Comparison of characteristic scales in medical ultrasound, and crustal geophysics.

		Medical Ultrasound	Crustal Geophysics
Propagation distance	L	250 mm	250 km
Useful waveform tomography frequencies	f	1 MHz	2 Hz
Approximate sound speed	c	1500 m/s	4000 m/s
Approximate wavelength	$\lambda = c/f$	1.5 mm	2 km
Number of wavelengths in target	$N_\lambda = L/\lambda$	167	125
Approximate Fresnel zone size	$\sqrt{\lambda L}$	20 mm	20 km

The approach used in this paper is a development referred to in geophysics as waveform tomography.[13–16] This approach is equivalent to diffraction tomography in a fully heterogeneous background medium. Waveform tomography owes its high resolution properties to the fact that the data are progressively matched to synthetic waveform data without recourse to ray-theoretical limitations. The synthetic data are generated using a highly accurate numerical simulation of the full, 2-D acoustic wave equation.[17, 18] All acoustic modes, including diffractions, guided waves, reflections and other scattering effects are automatically taken into account. The resolving power of waveform inversion methods has been characterized by several authors,[19–21] who demonstrate that waveform methods are expected to have a spatial resolving kernel of the order of the wavelength, λ, while traveltime methods are expected to be limited by the size of the Fresnel zone, $\sqrt{\lambda L}$, where L is the propagation distance between source and receiver. Wavelengths and Fresnel zone widths are provided in Table 1.[‡]

Waveform tomography of the inelastic attenuation parameter requires correctly modelling and inverting the amplitude effects of this parameter, which are strongly frequency dependent. Tarantola[22] gave the general formulation including both sound speed and attenuation parameters for the time domain, but this approach has not been applied in practice. Frequency domain approaches are more effective,[23, 24] and real data examples have also been published.[14, 25, 26] In the frequency domain, attenuation is parameterized using a complex-valued sound-speed parameter

$$v = v_r - i\frac{v_r}{2Q}, \tag{1}$$

[†]Smaller wavelengths are effectively limited by the intrinsic attenuation of the earth.

[‡]These scale represents the *order* of the resolution limitations; many methods can resolve down to a half, or even a quarter of these scales.

where v_r is the (real-valued) sound speed, and Q is the *quality factor*, a dimensionless parameter indicating the loss in energy per cycle.[14, 27] The *attenuation* is proportional to the inverse factor Q^{-1}, and to the frequency. In many materials Q is approximately constant with frequency, and that assumption is built into our reconstructions.

2. RING TRANSDUCER DATA

2.1. Transducer system

Data for this study were obtained using the CURE system[5] at the Karmanos Cancer Institute, Detroit, MI. The current prototype consists of a 20 cm diameter solid state ring transducer, with 256 active, non-beamforming transducers; data from each transducer location are available from all 256 elements around the ring. The breast is suspended in a water bath and surrounded by the ring transducers. The transducers have an effective elevation beam width of approximately 12 mm, making each scan approximately two-dimensional (2D), and a gantry system is used to create a stack of slices at different elevations. The transducers are driven at relatively low ultrasound frequencies, using a 1-cycle sinusoid at 1.5 MHz, with a source pulse containing frequencies between .5 and 2.5 MHz. For each dataset we obtained 256×256=65,536 waveforms, each containing 286 μs of full waveform data, sampled at 0.16 μs (approximately 0.2 Gbytes). The data were then translated from the native binary format of the system to the "Segy" format,[28] compatible with geophysical processing systems.

2.2. Datasets

Two datasets were used in this study of waveform tomography: The first is an ultrasound scan of the breast phantom shown schematically in Figure 1. This phantom consists of simulated breast tissue approximately 120 mm in diameter, with a 0.5 mm Polythene "skin", a subcutaneous layer of fat, a faceted parenchyma, and four simulated breast masses (two high sound-speed tumors, and two low sound-speed fat masses). Tumor and fat anomalies varied in size between 5 mm and 20 mm. The second dataset is a scan of an *in vivo* breast from a clinical study, exhibiting a large (30 mm diameter) tumor. We developed our workflow parameters using the data from the phantom, and then applied the identical workflow to the *in vivo* dataset.
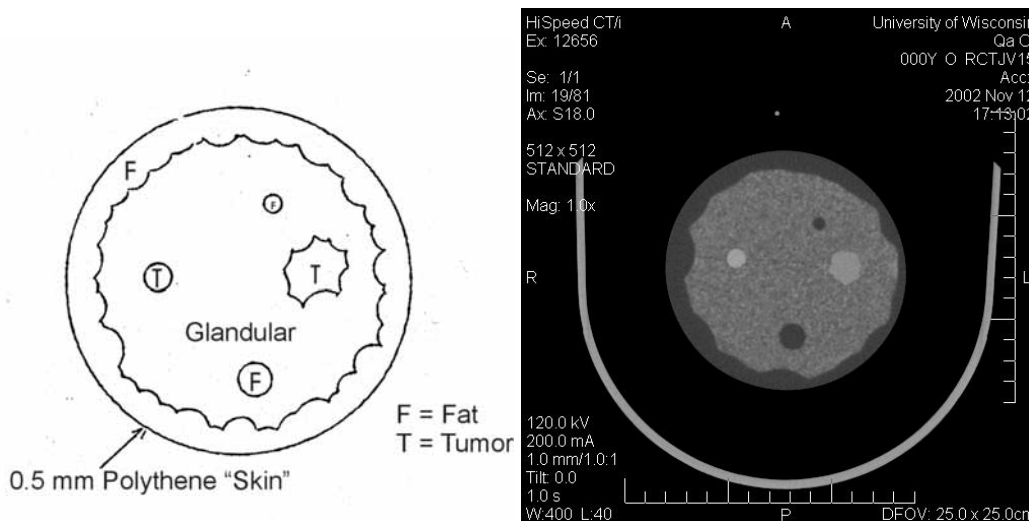

Figure 1. Left: Schematic design of the breast phantom. Right: x-ray CT scan of the breast phantom.

2.3. Waveform data

Figure 2 shows a typical scan from the ring transducer system, depicting data traces for all 256 transducers from a single transmit (a "common source gather"). Owing to the large variation in arrival times due to the ring geometry, the details of the transmission waveforms are somewhat difficult to perceive. In seismology, large

variations in arrival times are dealt with by plotting waveform data in "reduced time", $t - x/v_o$ where x is the source-receiver distance, and v_o is an appropriate, constant sound-speed used to remove much of the geometrical variation in the arrival times[§]. Figure 3 shows reduced time common source gathers for both the breast phantom data, and the *in-vivo* breast scan data. The time scale can be expanded on these reduced time plots, allowing us to clearly observe the transmission waveforms, including the diffractions from the edge of the breast phantom. On the *in vivo* data many more diffractions are present, indicating the presence of somewhat stronger sound speed heterogeneities in the breast. On these displays small traveltime shifts are are evident every 32 traces; this is a manifestation of the mechanical construction of the ring transducer system, in which the transducers are mounted on 32 element segments and assembled in 8 pieces. Minor geometric variations from a perfect circle thus occur.
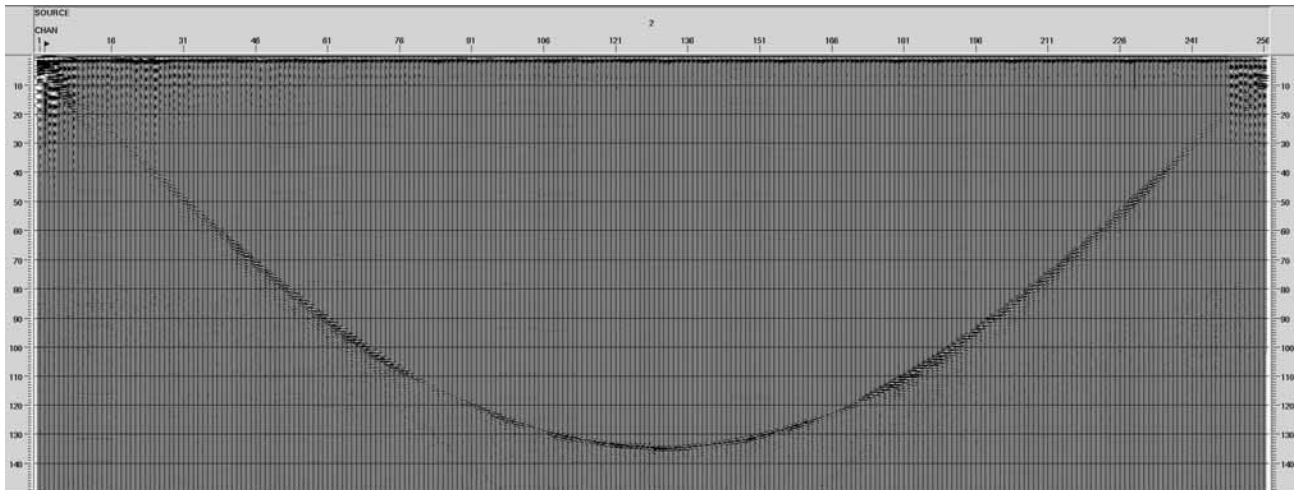

Figure 2. Ultrasound scan from a single transducer in the breast phantom showing the transmission arrivals around the circumference of the ring. Note the coherency of the arrivals and the crosstalk signals at early time on the near transducers. The Scholte wave arrival is just visible as a linear phase arriving after the transmission arrivals. The vertical axis is time in μsec.

3. TIME-OF-FLIGHT TOMOGRAPHY

For the waveform tomography approach to succeed a starting model is required that adequately predicts the first arrivals. The criterion usually given is that the starting model should predict the first arrivals to within a half-cycle[29] (0.625 μsec at 800 kHz). If this condition is not met, waveform tomography will converge to the wrong cycle of the waveform in parts of the data, an effect we refer to as a *cycle skip*.

In order to generate an appropriate starting model, we manually picked the arrival times for both datasets, using waveform displays such as those in Figure 3. The data were picked on the common source gathers, and subsequently triple checked for consistency in common receiver gathers, as well as common offset and common angle gathers. Each dataset required about 3 full working days to pick; approximately 50,000 traveltimes were retained per dataset. The accuracy of the manual picks was considered to be approximately 0.2 μsec. A number of dead channels were observed and eliminated from the traveltimes (and from the subsequent waveform data).

Time-of-flight inversion of the picked traveltimes was carried out using geophysical tomography software developed for cross-borehole surveys.[30] A variety of smoothing constraint levels were tested in order to obtain results that predicted the traveltimes to a root-mean-square error level of 0.1 μsec. Ray tracing is then carried out in the resulting sound speed model, and the procedure is repeated. These steps were repeated a total of three times to ensure the non-linearity of the approach was respected.

[§]In exploration seismology this is referred to as "linear moveout".

4. WAVEFORM TOMOGRAPHY

A comprehensive description of the waveform tomography approach has been given elsewhere;[15, 16, 31] in essence the method generates an iterative update to the starting sound-speed model (and, if desired, to the attenuation model), by minimizing the misfit between observed data and synthetic data generated by the method of finite differences in each successive model. In order to extract sound-speed information, transmission arrivals are strongly weighted during the inversion procedure. The process is carried out in the frequency domain: each frequency component of the data is matched by an equivalent frequency domain component of the synthetic data. Residuals are computed, and these residuals form the input for a "backpropagation" step in which the residuals are re-emitted inward into the target, and correlated with the propagated source terms. This creates a double-focusing effect, localizing the scattering points in a manner analogous to time-reversing mirrors.[32, 33]
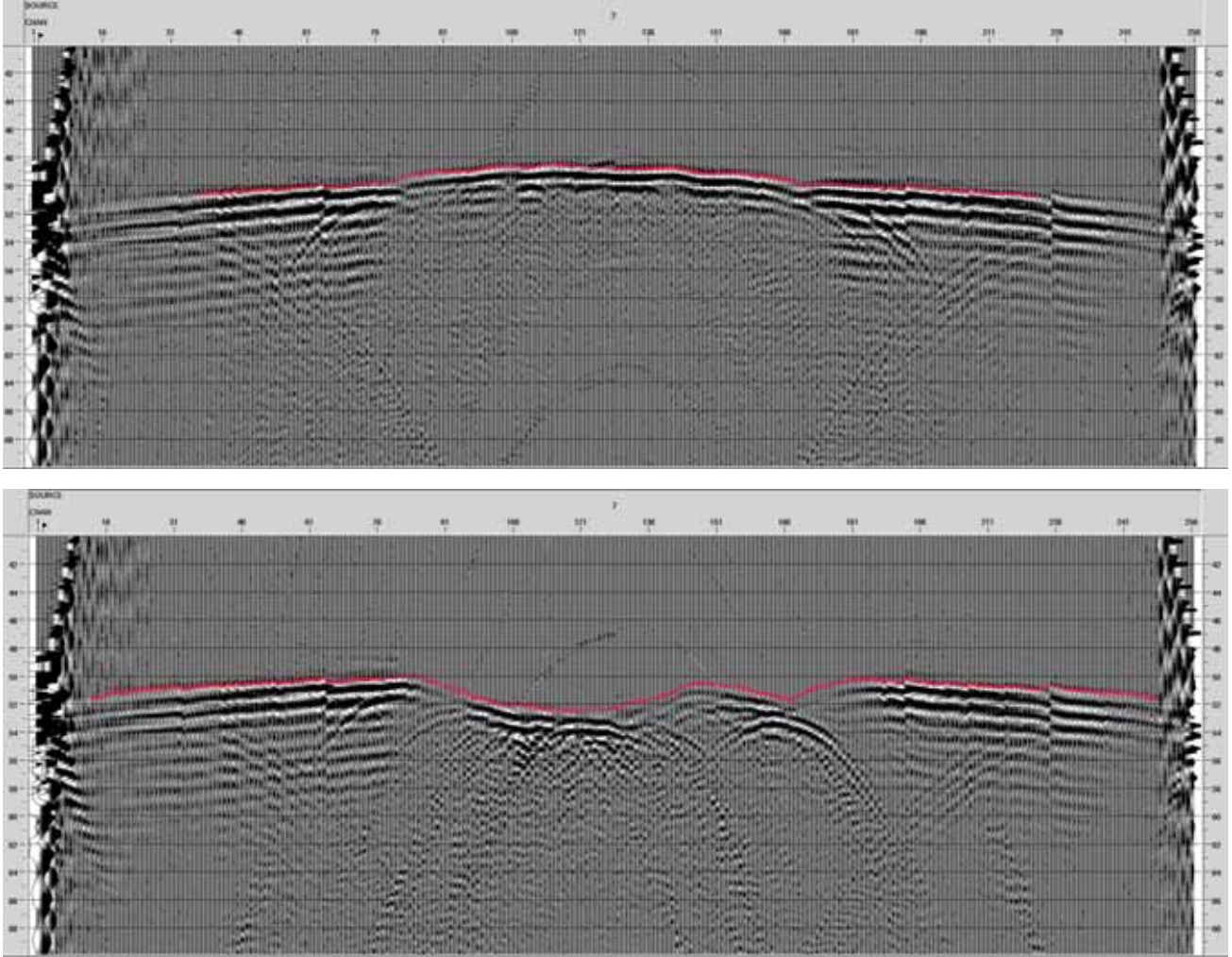

Figure 3. Top: An alternative display of the data from Figure 2, in which the data are plotted as a function of $t - x/v_o$, where $v_o = 1500$ m/s. Following a 50 μsec shift, and an expansion of the time scale the waveform details may be discerned. The departure from a straight line indicates the presence of material with a sound-speed different from that of water. As before, the crosstalk is visible; now the Scholte wave is easy to discern. We can now also see diffractions from the edges of the phantom. Bottom: A similar display of the *in-vivo* data, in which the breast structures create a complex first arrival waveform; diffraction patterns dominate the arrivals just after the transmission arrivals. In both plots the traveltime picks are indicated as small crosses on the waveforms. The vertical axis is time in μsec.

Mathematically, this allows us to efficiently construct the descent vector of an objective function. The method of conjugate gradients is used to accelerate convergence.

4.1. Waveform preprocessing

Before waveform tomography can be carried out, the data need to be reduced to a form suitable for the forward and inverse components of the algorithm. The pre-processing steps involve:

1. High cut (lowpass) filtering of data frequencies to a maximum of 800 kHz. This facilitates the processing of the lower frequency data components first, and allows a smaller computational grid to be used. At later stages this can be relaxed, and the highest data frequency components can in principle be included. A minimum phase Butterworth filter was applied with a 72 db/octave roll-off above 700 kHz.

2. Time windowing to remove any noise prior to the picked arrival times, and energy arriving later than 35 μsec subsequent to these arrivals. This removes late backscattered events from the data set, effectively forcing the algorithm to fit the earliest portions of the transmission waveforms. This operation too can be relaxed at later stages.

3. Gather-by-gather amplitude normalization. Each source gather is scaled to contain an overall root-mean-square amplitude of 1.0, following which the data are re-sorted into common receiver gathers and normalized once more. This dual normalization step removes most systematic amplitude variations between transducers.

4. Transformation of the data to the frequency domain, as required by the waveform tomography algorithm.

5. Removal of near transducer pairs from the files. These data points are overly sensitive to crosstalk, and the image is overly sensitive to minor timing and location errors in these data. We removed all transducer pairs closer than 75 mm to each other.

4.2. Extraction of frequency domain data

The waveform tomography algorithm operates on the waveform data one frequency at a time. We prepare the input data by transforming the filtered, windowed and scaled time domain data into a set of input data files, one per inversion frequency. Each of the 256×256=65,536 transducer pairs thus contributes a single, complex-valued data point to each data file. The generation of the frequency domain data is carried out using a standard discrete Fourier transformation of the form

$$F(\omega) = \sum_k f_k e^{i\omega k \Delta t}. \tag{2}$$

However, we actually carry out this summation (and subsequent finite difference modeling) using a complex-valued frequency ω given by

$$\omega = 2\pi f - \frac{i}{\tau}, \tag{3}$$

where f is the (real valued) frequency and τ is a *time damping* parameter used to reduce the weight of later arrivals in the data. The imaginary term in the circular frequency is equivalent to pre-multiplying the data by a term equal to $\exp(-t/\tau)$. For these examples a value of $\tau = 200\,\mu$s was used.

4.3. Source signature extraction

Before each pass of waveform tomography source signatures for all 256 transmitter elements are estimated from the data. Given the input data $d(\omega)$, and a starting sound-speed model, an initial set of synthetic data, $u(\omega)$ may be calculated by forward modelling. This allows us to extract an estimate of the source signature using[16]

$$s(\omega) = \frac{\langle u, d \rangle}{\langle u, u \rangle}, \tag{4}$$
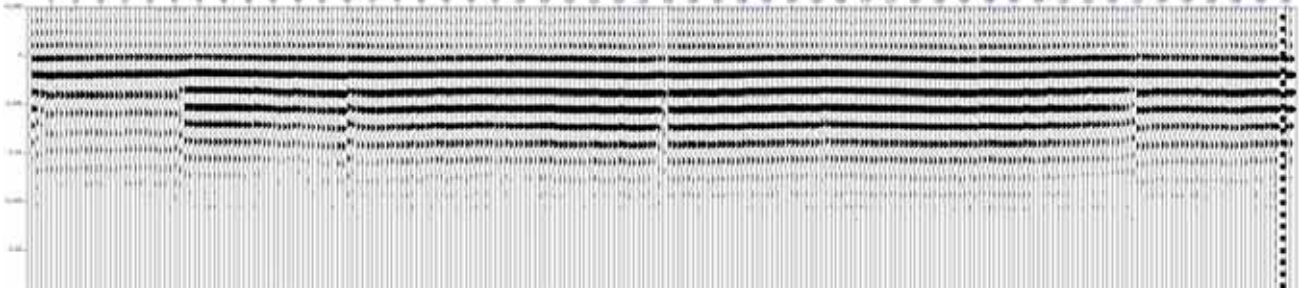
Figure 4. Source time signatures estimated for all 256 transducer elements in the ring transducer. The data have been previously filtered to a maximum frequency of 1 MHz. Transducer 254 was not functioning during this test.

where $\langle\rangle$ defines the inner product over all data points (equivalent to correlation in the time domain). The result, $s(\omega)$ is the complex-valued source function at the frequency, ω, following which the time-domain signatures may be found by Fourier synthesis. This operation may be applied to the data a single source gather at a time (yielding a source estimate for each gather separately), or to the entire dataset simultaneously (yielding only a single, best fit estimate of the source signature). Because of the traveltime steps observed in Figure 3 (associated with the 32-element transducer segments), it was decided to extract a separate source signature for each of the 256 transducer elements. The result of this calculation is shown in Figure 4; a small amount of variation is indeed evident between each 32-element segment.

4.4. 800 kHz Waveform tomography

Following waveform pre-processing, and time-of-flight tomography to establish a starting model, waveform tomography was applied to both datasets. The iterative procedure began with the 400 kHz data components, and proceeded through to 800 kHz in steps of 20 kHz. Three frequencies were used simultaneously per iteration, and five iterations of the conjugate gradient scheme were carried out before proceeding to the next group of three frequencies. A wavenumber-space filter was applied to each model update to restrict solutions to longer wavelengths (of the order of 2λ or larger, for each imaging frequency). Finally, a second pass was run through the data frequencies with a far less restrictive wavenumber filter (passing wavelengths as small as $\lambda/4$).

The sound speed waveform tomography results from the breast phantom are shown in Figure 6, together with the time-of-flight tomographic reconstruction used as a starting model on the same color scale, and a representative sound-speed profile through the phantom. Both reconstructions are slightly marred by the low sound-speed area at approximately 7 o'clock caused by the failure of a group of 8 transducers in this region. The reconstructions also show a faint correlation with the segmented structure of the ring transducer.

While the time-of-flight reconstruction yields a robust image of the phantom, some of the structures are poorly resolved: the polythene skin of the phantom is not evident, the faceted structure is only faintly apparent, and the interior anomalies are also rather faint. In contrast, the waveform tomography result contains high resolution structure that does not appear on the time-of-flight reconstruction, including a good image of the polythene skin (the nearly circular structure), the faceted nature of the subcutaneous fat interface, and each of the four anomalies. Unfortunately, the waveform tomography reconstruction also displays several artifacts (high and low sound-speed streaks), possibly associated with the traveltime discrepancies every 32-elements observed previously.
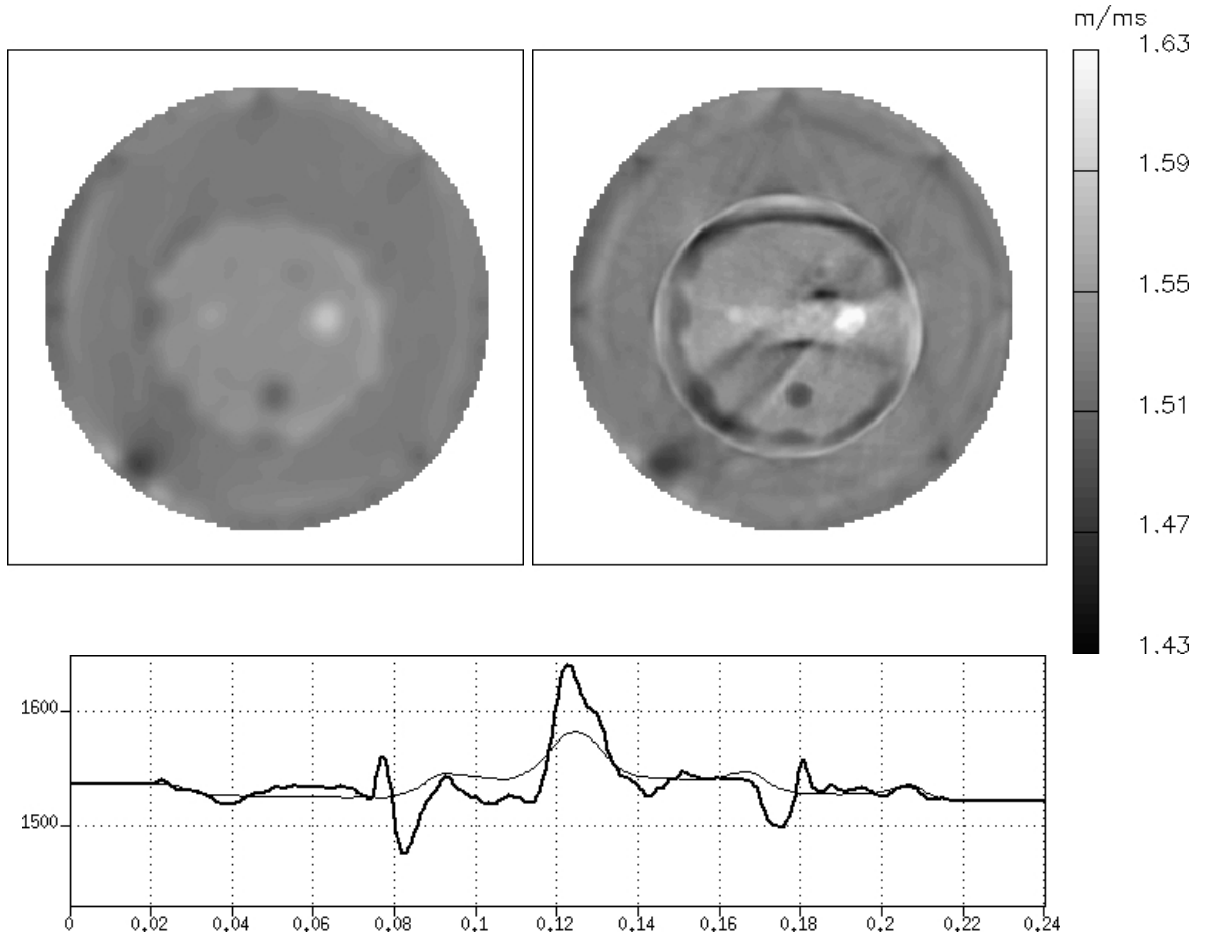
Figure 5. Sound speed images for the breast phantom. Left: Time-of-flight curved ray tomography. Right: Waveform tomography. The sound-speed graph shows a comparison of the sound speed from the time-of-flight reconstruction (thin line), and from the waveform tomography (thick line), taken along a line parallel to the vertical in both figures passing through the center of the large tumor anomaly.

The equivalent time-of-flight and waveform tomography reconstructions of the *in vivo* dataset are shown in Figure 6. Both reconstruction methods clearly show the enhanced sound speed of the tumor, however the waveform tomography image shows an improved localization of this structure. The waveform tomography reconstruction also is successful at providing a clear definition of the outer skin of the breast (not present in the time-of-flight reconstruction). Within the breast tissue there are additional sound-speed variations on the waveform tomography that resemble fibrous bands. Attenuation reconstructions for both datasets are shown in Figure 7. These images appear to respond directly to the high attenuation of the skin layer in both cases. On the *in vivo* attenuation image there is a region of high apparent attenuation that corresponds spatially to the location of the tumor.

5. DISCUSSION AND CONCLUSIONS

Waveform tomography appears to have great potential as a method for high-resolution, quantitative reconstruction of sound-speed and attenuation images in breast tissue. Certain difficulties in this prototype study have prevented us from obtaining artifact-free reconstructions. Specifically, the 32 segment pattern on the images is apparently due to some yet-to-be resolved problem with either the transducer geometry, the waveforms themselves, or the traveltime picking. This problem is not serious enough to prevent useful results, but it does lead to
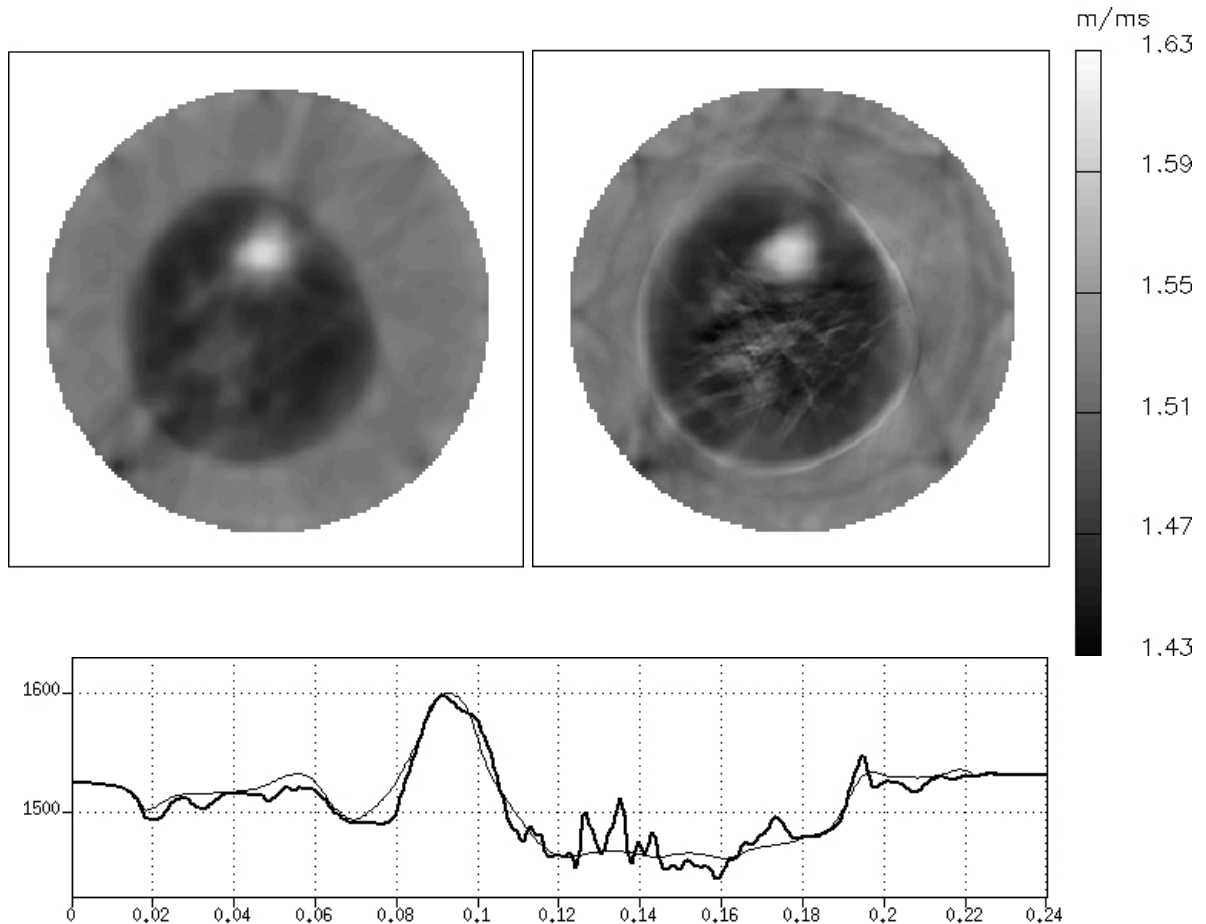
Figure 6. Sound speed images for the *in-vivo* data. Left: Time-of-flight curved ray tomography. Right: Waveform tomography. The sound-speed graph shows a comparison of the sound speed from the time-of-flight reconstruction (thin line), and from the waveform tomography (thick line), taken along a line parallel to the vertical in both figures passing through the center of the tumor.

artifacts in the waveform tomography that obscure some of the critical features of the breast phantom, making it difficult to see much improvement in the resolution of the smallest anomaly (the small fatty region). The problem does not seem to be as severe in the *in vivo* waveform tomography reconstruction.

The reconstructions of the breast phantom are helpful in evaluating the accuracy, resolution and reliability of waveform tomography: Waveform tomography does enhance the sound speed contrast of the largest anomalies in the phantom, both the high sound-speed tumor and the low sound-speed fatty region, and it also defines the edges of these more clearly. Furthermore, waveform tomography result resolves the polythene skin of the phantom extremely well, showing a nearly circular structure with a sharp increase in sound speed associated with the skin itself. There is also a decrease in sound speed just inside the skin that corresponds in detail with the geometry of the subcutaneous fat layer. These observations are further illustrated by the zoomed-in comparison shown in Figure 8, on which it is apparent that a resolution of the order of 2 mm was achieved.

These observations from the breast phantom allow us to view the reconstruction from the *in-vivo* data with some optimism. As with the phantom, the skin is clearly evident on the reconstruction. The internal structure appears better resolved, although it is difficult to know if the structure is totally artifact-free. It was noted during the reconstructions that the interior of the tumor structure itself did not change as the reconstruction proceeded, suggesting perhaps that little acoustic energy actually penetrated the tumor. The attenuation images
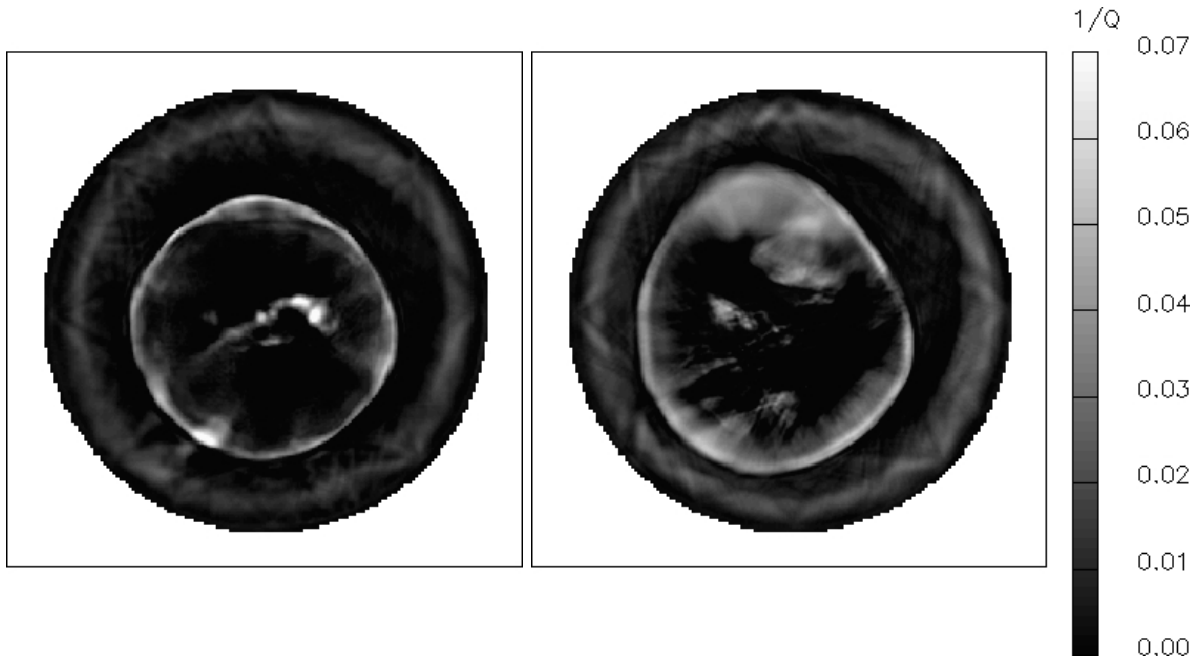
Figure 7. Attenuation images for the breast breast phantom (left), and the *in-vivo* dataset (right). Both images are presented in terms of $1/Q$, where Q is the dimensionless quality factor.

of the dimensionless Q factor from both datasets show little structure, other than at the interface between the skin and the subcutaneous fat layer. There is however a region of higher attenuation present in the interior of the *in vivo* example that corresponds to the spatial location of the tumor.
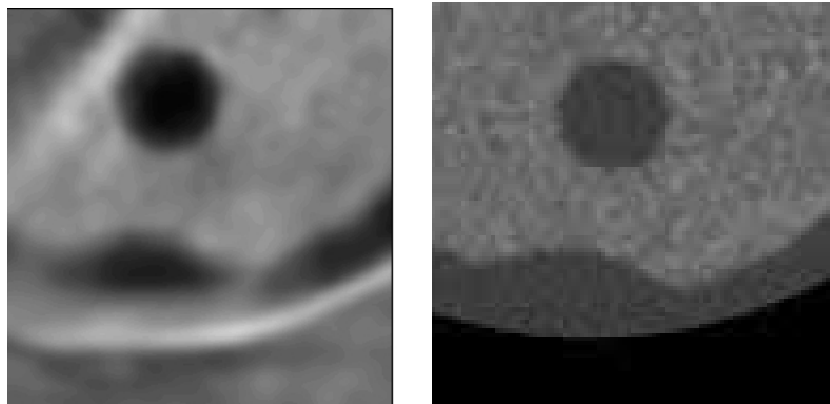

Figure 8. Detailed comparison of sound speed images from waveform tomography (left) and x-ray CT (right) in the breast phantom.

The potential for future applications of geophysical waveform tomography to medical ultrasound data seems assured. The reconstructions are accurate and well resolved down to sub-wavelength scales. At the same time, the waveform tomography approach appears less robust and more sensitive to calibration problems in geometry, timing and waveform amplitudes. It is anticipated that future research will lead to solutions to these problems, either with improved error-correction within the methodology, or with improved calibration of the transducer

systems, or both. This would lead the way forward to higher frequency reconstructions, with corresponding improvements in resolution approaching the sub-millimeter range. The method is limited in speed due to the requirement for manual traveltime picking of the waveforms, and due to the computational time required for the reconstructions. However, this is a prototype study and appropriate software engineering is likely to yield significant improvements on both of these requirements.

ACKNOWLEDGMENTS

REFERENCES

1. M. J. Berggren, S. A. Johnson, B. L. Carruth, W. W. Kim, F. Stenger, and P. K. Kuhn, "Ultrasound inverse scattering solutions from transmission and/or reflection data." International workshop on physics and engineering of computerized multidimensional imaging and processing., 1986, vol. 671, pp. 114-122, 1986.

2. P. Littrup, N. Duric, R. R. Leach, S. G. Azevedo, J. V. Candy, S. Johnson, G. Auner, J. Rather, and E. T. Holsapple, "Computerized Ultrasound Risk Evaluation (CURE) System: Development of combined transmission and reflection ultrasound with new reconstruction algorithms for breast imaging," *Acoustical Imaging* **26**, pp. 175–182, 2002.

3. P. Littrup, N. Duric, R. R. Leach Jr., G. Azevedo, C. J. V, T. Moore, D. H. Chambers, J. E. Mast, and E. Holsapple, "Characterizing tissue with acoustic parameters derived from ultrasound data." In *Ultrasonic Imaging and Signal Processing*, M. Insana and W.F. Walker, eds., *Proc. SPIE* **4687**, pp. 354-361, The International Society for Optical Engineering, (Bellingham, Washington), 2002.

4. N. Duric, P. Littrup, E. Holsapple, A. Babkin, R. Duncan, A. Kalinin, R. Pevzner, and M. Tokarev, "Ultrasound tomography of breast tissue." In *Ultrasonic Imaging and Signal Processing*, W.F. Walker and M. Insana, eds., *Proc. SPIE* **5035**, The International Society for Optical Engineering, (Bellingham, Washington), 2003.

5. N. Duric, E. Holsapple, B. Olsi Rama, C. Glide, P. Littrup, L. Poulo, A. Babkin, and R. Pevzner, "Detection of breast cancer with ultrasound tomography: First results with the Computed Ultrasound Risk Evaluation (CURE) Prototype," *Med. Phys.* **34(2)**, p. (accepted for publication), 2007.

6. N. Duric, P. Littrup, A. Babkin, D. Chambers, S. Azevedo, K. Arkady, R. Pevzner, M. Tokarev, E. Holsapple, O. Rama, and R. Duncan, "Development of ultrasound tomography for breast imaging: Technical assessment," *Med. Phys.* **32(5)**, pp. 1375–1386, 2005.

7. D. D. Dorney, J. L. Johnson, V. J. Rudd, R. G. Baraniuk, and W. W. Symes, "Terahertz reflection imaging using Kirchhoff migration," *Opt. Lett.* **26**, pp. 1513–1515, 2001.

8. L. Huang, N. Duric, and P. Littrup, "Ultrasonic breast imaging using a wave-equation migration method." In *Ultrasonic Imaging and Signal Processing*, W.F. Walker and M. Insana, eds., *Proc. SPIE* **5035**, pp. 432-439, The International Society for Optical Engineering, (Bellingham, Washington), 2003.

9. A. J. Devaney, "A filtered backpropagation algorithm for diffraction tomography," *Ultrasonic Imaging* **4**, pp. 336–350, 1982.

10. R. Wu and M. N. Toksöz, "Diffraction tomography and multisource holography applied to seismic imaging," *Geophysics* **52**, pp. 11–25, 1987.

11. A. Brenders and R. G. Pratt, "Full waveform tomography for lithospheric imaging: results from a blind test in a realistic crustal model," *Geophys. J. Int.* **168**, pp. 133–151, 2007.

12. A. Brenders and R. G. Pratt, "Efficient waveform tomography for lithospheric imaging: implications for realistic, two-dimensional acquisition geometries and low-frequency data," *Geophys. J. Int.* **168**, pp. 152–170, 2007.

13. R. G. Pratt and N. R. Goulty, "Combining wave equation imaging with traveltime tomography to form high resolution images from cross-hole data," *Geophysics* **56**, pp. 208–224, 1991.

14. Z. M. Song, P. R. Williamson, and R. G. Pratt, "Frequency-domain acoustic wave modeling and inversion of cross-hole data: Part II – Inversion method, synthetic experiments and real data results," *Geophysics* **60**, pp. 796–809, 1995.

15. R. G. Pratt, C. Shin, and G. Hicks, "Gauss-Newton and full Newton methods in frequency-space seismic waveform inversion," *Geophys. J. Int.* **133**, pp. 341–362, 1998.

16. R. G. Pratt, "Seismic waveform inversion in the frequency domain, Part 1: Theory and vertification in a physical scale model," *Geophysics* **64**, pp. 888–901, 1999.

17. R. G. Pratt and M. H. Worthington, "Inverse theory applied to multi-source cross-hole tomography. Part I: Acoustic wave-equation method," *Geophysical Prospecting* **38**, pp. 287–310, 1990.

18. C. H. Jo, C. S. Shin, and J. H. Suh, "Design of an optimal 9 point finite difference frequency-space acoustic wave equation scheme for inversion and modeling," *Geophysics* **61**, p. 329, 1996.

19. P. R. Williamson, "A guide to the limits of resolution imposed by scattering in ray tomography," *Geophysics* **56**, pp. 202–208, 1991.

20. P. R. Williamson and M. H. Worthington, "Resolution in ray tomography due to wave behaviour; Numerical experiments," *Geophysics* **58**, pp. 727–735, 1993.

21. G. T. Schuster, "Resolution limits for crosswell migration and traveltime tomography," *Geophys. J. Int.* **127**, pp. 427–440, 1996.

22. A. Tarantola, "Theoretical background for the inversion of seismic waveforms, including elasticity and attenuation," *Pure and Applied Geophysics* **128**, pp. 365–399, 1988.

23. R. G. Pratt, "Frequency domain elastic wave modeling by finite differences: A tool for cross-hole seismic imaging," *Geophysics* **55**, pp. 626–632, 1990.

24. Q. Liao and G. A. McMechan, "Multifrequency viscoacoustic modeling and inversion," *Geophysics* **62**, pp. 1371–1378, 1996.

25. G. Hicks and R. G. Pratt, "Reflection waveform inversion using local descent methods: estimating attenuation and velocity over a gas sand deposit," *Geophysics* **66**, pp. 598–612, 2001.

26. R. G. Pratt, F. Hou, K. Bauer, and M. H. Weber, "Waveform tomography images of velocity and inelastic attenuation from the Mallik 2002 crosshole seismic surveys," 2005.

27. K. Aki and P. G. Richards, *Quantitative seismology, theory and methods*, W. H. Freeman and Co, 1980.

28. K. M. Barry, D. A. Cavers, and C. W. Kneale, "Recommended standards for digital tape formats," *Geophysics* **40**, pp. 344–352, 1975.

29. L. Sirgue and R. G. Pratt, "Efficient waveform inversion and imaging: a strategy for selecting temporal frequencies," *Geophysics* **69**, pp. 231–248, 2004.

30. R. G. Pratt and C. H. Chapman, "Traveltime tomography in anisotropic media–II. Application," *Geophysical Journal International* **109**, pp. 20–37, 1992.

31. R. G. Pratt and R. M. Shipp, "Seismic waveform inversion in the frequency domain, Part 2: Fault delineation in sediments using crosshole data," *Geophysics* **64**, pp. 902–914, 1999.

32. M. Fink, "Time-reversal mirrors," *J. Phys. O: Appl. Phys.* **26**, pp. 1333–1350, 1993.

33. L. Huang, N. Duric, and P. Littrup, "Breast imaging with time-reversed ultrasound." In *Ultrasonic Imaging and Signal Processing*, S. Smelianov and W.F. Walker, eds., *Proc. SPIE* **6147**, pp. 156-167, The International Society for Optical Engineering, (Bellingham, Washington), 2006.